

Porous TiO₂/C Nanocomposite Shells As a High-Performance Anode Material for Lithium-Ion Batteries

Wenshou Wang,[†] Qina Sa,[‡] Jihua Chen,[§] Yan Wang,[‡] Heejung Jung,[⊥] and Yadong Yin^{*,†}

[†]Department of Chemistry and [⊥]Department of Mechanical Engineering, University of California, Riverside, California 92521, United States

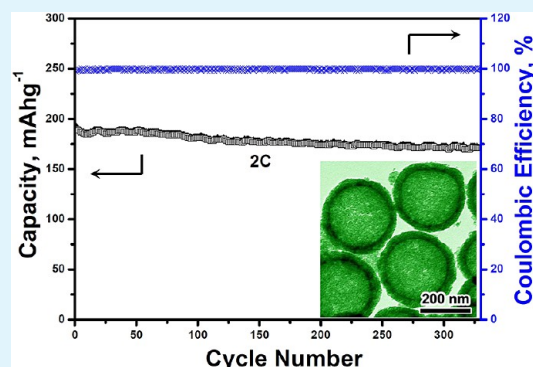
[‡]Department of Mechanical Engineering, Worcester Polytechnic Institute, 100 Institute Road, Massachusetts 01609, United States

[§]Center for Nanophase Materials Sciences, Oak Ridge National Laboratory, Oak Ridge, Tennessee 37831, United States

S Supporting Information

ABSTRACT: Porous TiO₂/C nanocomposite shells with high capacity, excellent cycle stability, and rate performance have been prepared. The synthesis involves coating colloidal TiO₂ nanoshells with a resorcinol-formaldehyde (RF) layer with controllable thickness through a sol-gel-like process, and calcining the composites at 700 °C in an inert atmosphere to induce crystallization from amorphous TiO₂ to anatase and simultaneous carbonization from RF to carbon. The cross-linked RF polymer contributes to the high stability of the shell morphology and the porous nature of the shells. A strong dependence of the capacity on the amount of incorporated carbon has been revealed, allowing the optimization of the electrode structure for high-rate cell performance.

KEYWORDS: TiO₂/C nanocomposite shells, porous, resorcinol-formaldehyde (RF) layer, carbon-coating, anode, lithium-ion battery



INTRODUCTION

Titanium dioxide (TiO₂) is a promising anode material for lithium-ion battery because of its merits in terms of safety, cost, environmental friendliness, and chemical stability.^{1–3} However, the poor rate capability of TiO₂ electrode, which results from their intrinsically low Li-ion diffusivity ($\sim 1 \times 10^{-15}$ to 1×10^{-9} cm² s⁻¹) and low electronic conductivity ($\sim 1 \times 10^{-12}$ to 1×10^{-7} S cm⁻¹), limits their practical use.^{1–3} Considerable efforts have been made to engineer the structures of TiO₂ at the nanoscale to enhance the rate performance, for example, by producing porous or hollow nanostructures which possess many advantages such as high contact area between electrolyte and electrode, short diffusion distance for Li⁺ transport, and the ability to accommodate strain during cycling.^{4–7} To promote Li-ion diffusion and electron transport, conducting materials such as carbon are sometime introduced into the TiO₂ nanostructures.^{8–11} Conventionally, carbon incorporation is achieved by heating mixtures of metal salts and carbon precursors such as typically used glucose;^{12,13} however, it is difficult to ensure controllable and continuous distribution of carbon within the electrode materials.

In this work, we report the synthesis of a new type of porous TiO₂ nanoshells with precisely controlled carbon incorporation for highly reversible lithium storage. This unique structure combines the advantages of porous shells and carbon incorporation and significantly improves the rate performance of TiO₂ electrodes. The synthesis involves coating a resorcinol-formaldehyde (RF) layer on sol-gel derived hollow TiO₂

spheres through another sol-gel like process, and then calcining the samples at high temperature to carbonize the cross-linked polymer and crystallize the TiO₂ shell. The advantages of this carbon incorporation route over the previously reported hydrothermal methods include precise control over carbon loading and distribution, simple synthetic procedure, and high reproducibility. The presence of the polymer shell limits the extensive crystallization of the TiO₂ during calcination and helps to maintain a continuous and porous shell structure which is beneficial to the diffusion of the lithium ions. With the ability to precisely control the carbon incorporation, we have been able to optimize the structure of the TiO₂/C nanocomposites and produce anode materials showing significantly improved electrochemical performance with a high specific capacity of 288.2 mA h g⁻¹ at a current rate of 0.1C. The rate capability and cycling performance are also greatly enhanced, showing capacities of 189.6 mA h g⁻¹ at 2C and 139.9 mA h g⁻¹ at 10C, and a well-maintained capacity of 170.8 mA h g⁻¹ after cycling for 330 times at a current rate of 2C.

RESULTS AND DISCUSSION

The synthesis of porous TiO₂/C nanoshells mainly consists of two steps. The first step is the preparation of amorphous TiO₂

Received: June 18, 2013

Accepted: July 5, 2013

Published: July 5, 2013

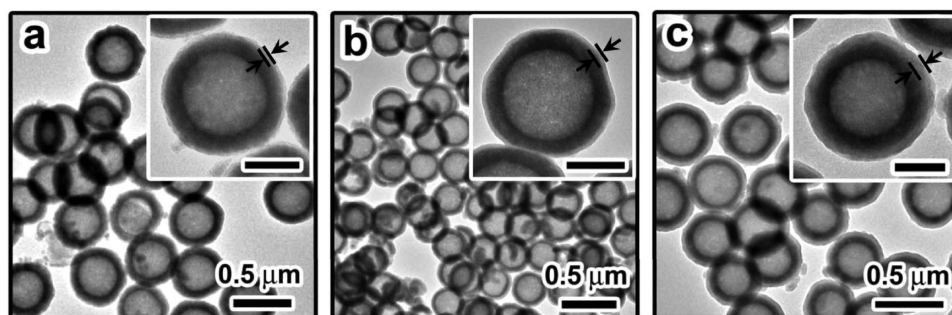


Figure 1. TEM images of amorphous TiO_2/RF nanoshells with different thicknesses of RF layers obtained by using (a) 100 mg of resorcinol and 140 μL of formaldehyde, (b) 250 mg of resorcinol and 350 μL of formaldehyde as precursors, and (c) two cycles of the RF coating procedure described in b. For clarity, the RF layers have been labeled in the insets. Scale bar in insets: 200 nm.

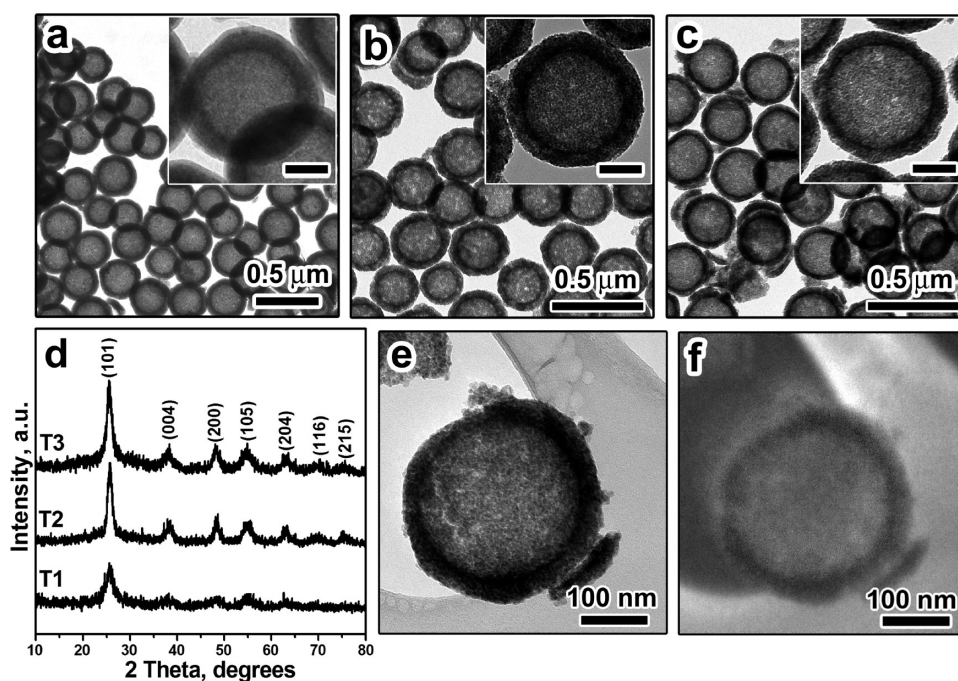


Figure 2. (a–c) TEM images of porous TiO_2/C shells: (a) sample T1, (b) sample T2, and (c) sample T3; (d) XRD patterns of the corresponding samples; (e) TEM image and (f) carbon mapping of an individual TiO_2/C shell from sample T3. Scale bars in insets: 100 nm.

nanoshells by coating TiO_2 on colloidal SiO_2 spheres through a sol–gel process, followed by selective etching of the SiO_2 sacrificial templates, as reported in our recent publication.¹⁴ The second step consists of coating a RF layer on the TiO_2 shells through sol–gel-like process by reacting resorcinol and formaldehyde in the presence of ammonia and cetyltrimethylammonium bromide (CTAB), and calcination at 700 °C to induce phase transformation from amorphous TiO_2 to anatase and carbonization from RF to carbon.^{15,16} The involved sol–gel and calcination processes are simple, inexpensive, flexible, scalable, and highly reproducible.

The sol–gel-like process allows convenient deposition of a RF polymer layer with a precisely controlled thickness on the surface of amorphous TiO_2 nanoshells. Figure 1 shows the TEM images of amorphous TiO_2/RF shells coated with RF layers of different thicknesses. All samples are composed of uniform spherical nanoshells each consisting of an amorphous TiO_2 hollow core and a polymeric shell, as marked in Figure 1. The thickness of RF layer can be easily adjusted by varying the amount of precursors of resorcinol and formaldehyde used in the synthesis. For example, the thickness of RF is ~ 10 nm

when 100 mg of resorcinol and 140 μL of formaldehyde are used (Figure 1a), which increases to ~ 15 nm when the amount of precursors change to 250 mg of resorcinol and 350 μL of formaldehyde (Figure 1b). In addition, a thicker RF layer can be conveniently achieved by carrying out multiple coating steps, for example, two cycles of coating increases the RF thickness to ~ 40 nm (Figure 1c).

To produce porous TiO_2/C composite shells, we calcined the amorphous TiO_2/RF spheres in argon at 700 °C to induce the crystallization of amorphous TiO_2 to anatase and the conversion of RF to carbon. We designate the TiO_2/C samples prepared by starting with 250, 100, 25, and 6.25 mg of resorcinol as T1, T2, T3, and T4. Because of its relatively thick coating of RF, sample T1 clearly shows a uniform layer of carbon covering the surface of TiO_2 nanoshells (Figure 2a). No collapsed or broken shells can be seen due to the mechanical reinforcement of the carbon coating. When samples with thinner RF coatings are carbonized, they are still composed of uniform nanoshells (samples T2 and T3, Figure 2b, c) but no apparent carbon layer can be detected even in high-magnification TEM images. Close examination reveals that

the grain size of TiO₂ in the nanoshells increases with decreasing thickness of original RF coating. Nanoscale pores can be clearly observed for samples with less original RF coating probably because of less confinement to the growth of TiO₂ grains. Such pores are highly desirable for enhanced Li-ion diffusion and consequently the overall rate capabilities due to shorter diffusion lengths.

Figure 2d shows the X-ray powder diffraction (XRD) patterns of the calcined porous nanoshells with different loading amounts of carbon. All of the observed diffraction peaks can be perfectly indexed to anatase TiO₂ with cell constants of $a = 3.7852 \text{ \AA}$ and $c = 9.5139 \text{ \AA}$ (JCPDS card no. 21-1272). The strong and sharp diffraction peaks indicate good crystallinity of the as-synthesized products, while the significant broadening of the peaks suggests small TiO₂ grain sizes. The diffraction peaks become sharper as the thickness of the original RF coating decreases, suggesting that the polymer layer can effectively limit the grain growth of TiO₂. The average grain sizes of the porous TiO₂/C nanoshells, as estimated using Scherrer's formula, are ~ 11 , 10, and 8 nm, respectively, with increasing RF thicknesses. A similar limiting effect has also been observed when sintering TiO₂ shells covered by a silica layer.^{14,17} It should be noted that only the anatase phase of TiO₂ can be detected in the sample calcined at $\sim 700 \text{ }^\circ\text{C}$, whereas rutile starts to appear when the sample is treated at $\sim 800 \text{ }^\circ\text{C}$.

To characterize the distribution of carbon within the shells, we mapped the elemental distribution of carbon in the calcined shells of sample T3, and compared the result with regular TEM imaging (Figure 2e, f). In the carbon mapping, brighter regions contain more carbon. The carbon mapping on ultrathin carbon/holey carbon substrate was collected with a three-window method to be quantitative (the background of ultrathin carbon from substrate has been subtracted). A strong carbon signal can be detected throughout the shells, especially in the region between holey carbon substrate and hollow shell, as shown in Figure 2f, suggesting the existence of carbon materials in the TiO₂ porous network. In our earlier study of silica coating on TiO₂ shells, we have noticed that the deposited silica species can penetrate into the porous network of amorphous TiO₂ shells, and therefore significantly affects the crystallization of TiO₂ during calcination.¹⁴ We believe RF may behave similarly and penetrate into the TiO₂ shells, leading to incorporation of a considerable amount of carbon beyond the TiO₂ surface.

Raman spectroscopy was further used to characterize the ordering of the carbon of sample T3 (see the Supporting Information). The peaks between 100 and 700 cm⁻¹ in the Raman spectrum are the typical features of anatase TiO₂.¹² The characteristic peak located at $\sim 1345 \text{ cm}^{-1}$ in the Raman spectrum corresponds to the D band of carbon, suggesting the disordered carbon. The peak at 1598 cm⁻¹ corresponds to G band of carbon, indicating the existence of sp² graphitic carbon. Compared to the single crystal of graphite (1575 cm⁻¹), the G band of sample T3 shifts to high wave numbers, which is probably due to the formation of thin carbon shell on TiO₂. Graphitization of the carbon is believed to be beneficial the electrochemical performance by enhancing the conductivity of the shells.

Thermogravimetric analysis (TGA) of sample T3 indicates 9.3 wt % of carbon loading (see the Supporting Information, Figure S2), which is slightly higher than that achieved by using glucose as precursor.¹² It is interesting to note that in our case,

even though the carbon loading is higher, we do not observe an obvious layer of carbon coating on the surface of TiO₂ shells as in the case of using glucose, suggesting deep penetration of carbon species into the porous TiO₂ network. However, it is still reasonable to argue that the near-surface region of the TiO₂ shells contains more carbon than inside regions, as evidenced by the gradual decrease in brightness from the surface to the inside of the shell in elemental mapping. Nitrogen adsorption-desorption isotherm measurement of the sample T3 presents a typical type IV hysteresis loop with a Brunauer-Emmett-Teller (BET) surface area of 96.8 m²/g (see the Supporting Information, Figure S3), a number comparable to that of the mesoporous TiO₂ shells with similar crystallinity reported previously in our group by combining silicate protection and calcination.¹⁸ Although there is no sharp distribution peak in the BJH pore size distribution curve, sample T3 shows pores with sizes in the range of 1–5 nm. The adsorption-desorption isotherm results confirm the mesoporous nature of the TiO₂/C composite shells, which is believed to benefit the fast diffusion of the lithium ions.

Figure 3a shows the representative discharge/charge voltage profiles of the electrode made of porous TiO₂/C nanoshells with thin carbon layer (sample T3) at a current rate of 0.1 C within a cutoff voltage window of 1.0–3.0 V, which are consistent with typical discharge/charge voltage profiles of TiO₂. All the capacities are calculated based on the mass of TiO₂/C nanocomposites. The porous TiO₂/C nanoshells can achieve a high lithiation capacity of 415.5 mA h g⁻¹ and a delithiation capacity of 272.3 mA h g⁻¹ in the first cycle. The first discharge curve at 0.1 C shows a potential plateau at around 1.75 V and a sloped region of 1.75–1.0 V, and voltage plateaus at around 1.88 V in the first charge process. The voltage plateaus at 1.75 and 1.88 V correspond to lithium-ion intercalation into and deintercalation from the interstitial octahedral sites of anatase TiO₂, respectively.¹⁹ The discharge capacity originates from the reduction of Ti_(IV) to Ti_(III) with the intercalation of the lithium ion, whereas the charge capacity originating from the oxidation of titanium.¹⁹ The Li insertion/extraction reaction in TiO₂ can be written as: $\text{TiO}_2 + x\text{Li}^+ + xe^- \leftrightarrow \text{Li}_x\text{TiO}_2$, where x is the amount of inserted Li⁺ in anatase TiO₂.²⁰ The large capacity loss ($\sim 34.5\%$) in the first cycle is mainly attributed to the interfacial reaction between TiO₂ and the electrolyte, which is common to most lithium intercalation hosts. Despite the capacity decay after the first cycle, the porous TiO₂/C nanoshells maintain a high discharge and charge capacities of 288.2 and 260.1 mA h g⁻¹ in the second cycle and show very good capacity retention thereafter (Figure 3a). The charge-discharge voltage profiles of first cycle at different current density are shown in Figure 3b. The first discharge capacity at different current density of 0.1, 0.33, 0.5, 1, 2, 5, and 10 C are 415.5, 254.1, 237.9, 223.4, 204.2, 189.6, 168.8, and 139.9 mA h g⁻¹, respectively. As expected, although the capacity and the potential plateau both decrease with increasing current density, a high capacity of 189.6 mA h g⁻¹ is still achieved at 2C. Remarkably, the sample demonstrates excellent capacity retention even cycled at 2C for 330 times, demonstrating excellent cycling performance at high rates (Figure 3c). The porous TiO₂/C nanoshells are able to deliver a reversible Li storage capacity of 189.6 mA h g⁻¹ at the first cycle, and 170.8 mA h g⁻¹ can still remain after over 330 cycles, with a capacity loss of only 9.9%. The superior cycling performance can be attributed to the structural stability of porous TiO₂/C nanoshells due to the good accommodation to volume/strain

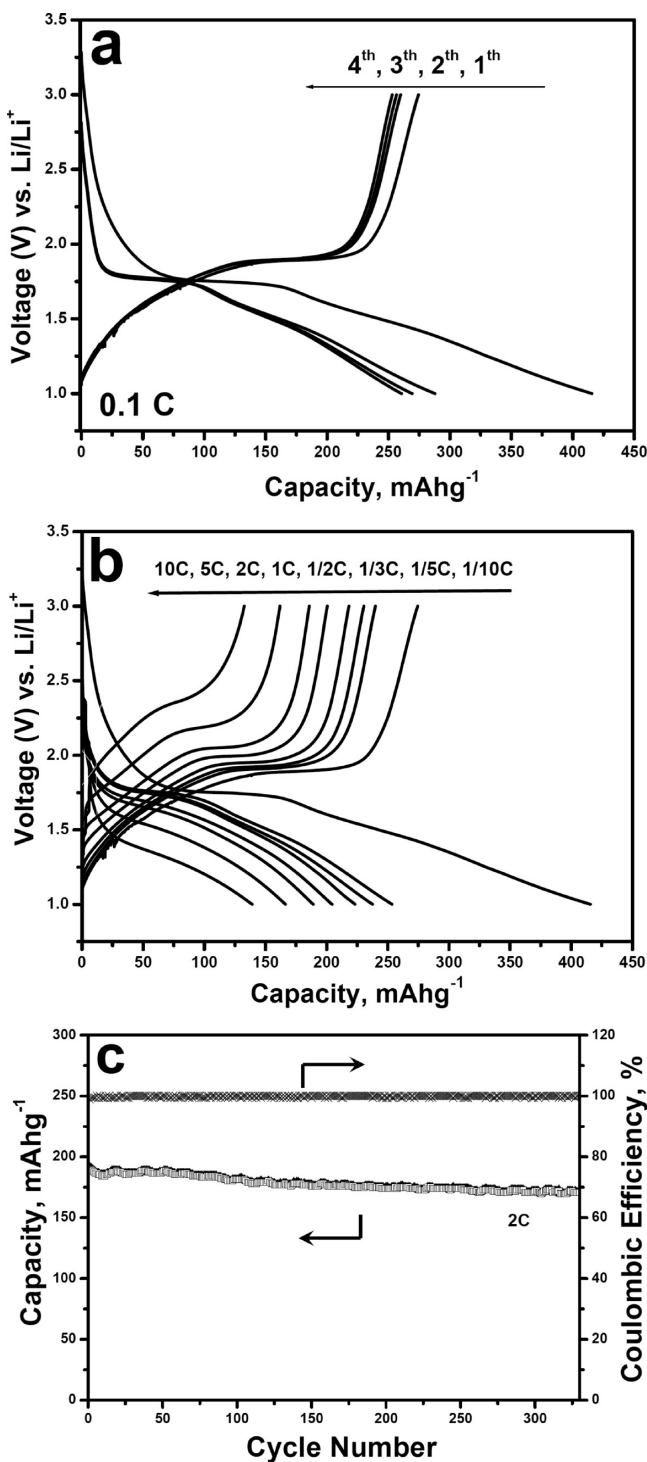


Figure 3. (a) Discharge–charge voltage profiles at a current rate of 0.1C, (b) the first discharge–charge voltage profiles at different current density, and (c) cycling performance of the porous TiO₂/C nanoshells cycled at a constant current density of 2C and the corresponding Coulombic efficiency. Voltage range is 1.0 – 3.0 V vs. Li/Li⁺.

changes during lithium insertion–extraction. Also shown in Figure 3c, the Coulombic efficiency remains at nearly 100% during the cycling process, indicating highly reversible lithium insertion/extraction kinetics. The performance of our porous TiO₂/C nanoshells is superior to that of many TiO₂ hollow or porous nanostructures reported previously, including those with carbon coating.^{8–10,2f–23}

The porous TiO₂/C composites containing different amount of carbon (samples T2, T3, and T4), were tested under the same conditions to evaluate the effect of carbon loading on the performance. Figure 4a compares their rate performance at

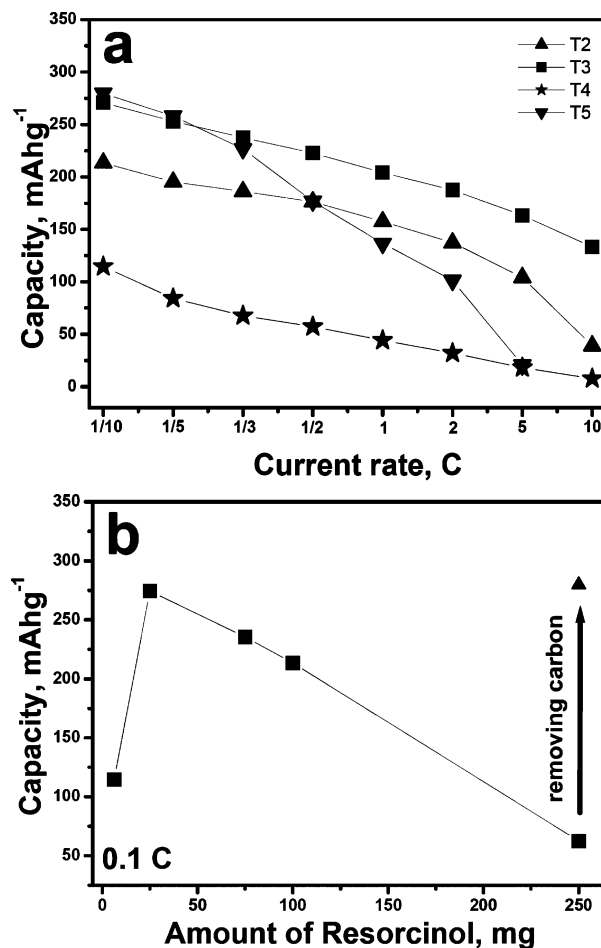


Figure 4. (a) Rate performance and (b) capacity of porous TiO₂/C nanoshells as a function of the amount of resorcinol obtained at a current rate of 0.1C. Voltage range is 1. – 3.0 V vs. Li/Li⁺.

different current rates. Sample T3 exhibits the best rate performance, which shows about 21 and 200% enhanced capacity compared with that of samples T2 and T4 at all current density. It is clear that an excessively thick carbon coating on TiO₂ nanoshells, like the case of sample T2, would act as a barrier for Li⁺ diffusion, which decreases the rate performance. The inclusion of much less carbon (sample T4) leads to aggregation of the nanoshells during calcination and consequently rapid fading of the capacity. As summarized in Figure 4b, the higher rate capability of the sample T3 clearly demonstrates that the incorporation of carbon with an appropriate amount facilitates excellent cycling stability and high rate performance. To further demonstrate the importance of carbon incorporation, we also tested porous TiO₂ nanospheres after removing carbon from the composite T1 by additional calcination in air (sample T5). It is clear that T3 and T5 samples have similar capacities at low current densities, such as 1/10, 1/5, and 1/3C, but differ significantly at high current densities. The capacity of sample T5 decreases steeply from 226.8 to 18.2 mA h g⁻¹ with an increasing density from 1/3 to 5C, showing a capacity loss of ~92%. In contrast, sample T3

shows a capacity loss of only 31%, from 237.5 to 163.5 mA h g⁻¹ when the current density increases from 1/3 to 5C. The higher capacity of sample T3 than sample T5 at higher current density can be attributed to the faster electron transport enabled by the incorporation of carbon.

Our results clearly suggest the enhancement in the high rate cell performance when an appropriate amount of carbon is introduced into the porous TiO₂ hollow shells: (i) it limits the growth of TiO₂ during calcination, leading to small grains, mesoscale porosity, and considerably high surface area; (ii) the carbon layer is incorporated into the porous network of the TiO₂ shells, significantly enhancing the electron transport of the electrode; and (iii) the porous structure and the hollow shell morphology are well maintained so that the structural strain and volume change associated with the repeated Li⁺ insertion/extraction processes could be buffered effectively. As a result, significant improvement in rate capability and cycling stability could be achieved through the synergistic effects of the porous shell geometry and the incorporation of conductive carbon.

CONCLUSIONS

In summary, controllable incorporation of carbon species into porous TiO₂ hollow shells has been successfully achieved through multiple sol-gel processes and a subsequent carbonization process, producing porous TiO₂/C nanocomposites with significantly improved cycling performance for Li ion storage and excellent rate capability up to 10C. A coating of cross-linked polymer, which serves as the precursor to carbon, was found to significantly limit the crystallization of TiO₂ and therefore help to not only maintain the shell morphology but also produce smaller crystal grains and mesoscale pores that are beneficial to the diffusion of the lithium ions. A strong dependence of the cell performance on the amount of carbon incorporation has also been revealed, enabling the rational design of future electrode materials involving nanoscale composites of metal oxides and carbon for high-performance lithium-ion batteries.

EXPERIMENTAL METHODS

Materials Synthesis. Amorphous TiO₂ hollow nanoshells were synthesized by coating colloidal silica spheres (typically ~400 nm in diameters) with a layer of TiO₂ and then removing the silica core through chemical etching with a NaOH solution.¹⁴ The samples were washed by a diluted hydrochloric acid solution to remove the sodium residue.¹⁸ In a typical process for coating TiO₂ shells with RF, ~200 mg of amorphous TiO₂ nanoshells was sequentially mixed with 145 mL of distilled water, 5 mL of CTAB aqueous solution (0.01 M), 0.5 mL of ammonia aqueous solution (28 wt %), 250 mg of resorcinol, and 350 μL of formaldehyde at 50 °C. After reaction of 1 h at 50 °C, the solid product was collected by centrifugation, washed with water and ethanol, and air-dried at 80 °C for several hours. The as prepared TiO₂/RF composites were finally calcined under an argon atmosphere at 700 °C for 4 h, producing TiO₂/C hollow particles with porous shells. The thickness of the RF coating and subsequently the carbon loading can be varied by controlling the amount of resorcinol. A control sample with carbon removed by calcining sample T1 at 500 °C in air is designed as T5.

Materials Characterization. Crystal structure of the products was measured on a Bruker D8 Advance X-ray Diffractometer (XRD) with Cu K_α radiation ($\lambda = 1.5418 \text{ \AA}$). Morphology and size of the products were characterized by using a Tecnai T12 transmission electron microscope (TEM). Carbon mapping were conducted using a Zeiss Libra 120 with an Omega energy filter. Energy filtered TEM experiments were performed at 120 kV with an emission current of 6 μA in order to minimize electron-beam-induced sample damage. The surface area and porosity of the products were estimated by measuring the nitrogen adsorption-desorption isotherms on a NOVA 4200e surface area & pore size analyzer. TGA analysis was performed on a Seiko TG/DTA 220 with a heating rate of 10 °C/min under air. Raman spectrum was measured on a Renishaw DXR Raman spectroscopy system with a 532 nm laser source (8 mW excitation power, 100× objective lens).

Electrochemical Measurement. The electrochemical measurements were carried out using two-electrode Swagelok-type cells. The working electrode (diameter: 0.25 in.) is consisted of active material (porous TiO₂/C nanoshells), carbon black (Super-P), and polymer binder (polyvinylidene fluoride) in a weight ratio of 80:10:10. The electrodes typically have a loading mass of 2 mg. Metallic lithium was used as both the counter electrode and reference electrode. LiPF₆ electrolyte solution (1M) in ethylene carbonate (EC), diethyl carbonate (DEC), and dimethyl carbonate (DMC) (1:1:1) was used as the electrolyte. Cell assembly was carried out in an Ar-filled glovebox with moisture and oxygen concentrations below 1.0 ppm. The galvanostatic charge/discharge tests were performed on a galvanostat/potentiostat/impedance analyzer (Biologic VMP3). Electrochemical cells were charged and discharged at constant current with different rates in a voltage range of 1.0–3.0 V.

ASSOCIATED CONTENT

Supporting Information

Raman, TGA, N₂ adsorption-desorption isotherm measurements of the electrode materials. This material is available free of charge via the Internet at <http://pubs.acs.org>.

AUTHOR INFORMATION

Corresponding Author

*E-mail: yadong.yin@ucr.edu. Tel: +1-951-827-4965. Fax: +1-951-827-4713.

Notes

The authors declare no competing financial interest.

ACKNOWLEDGMENTS

This project is financially supported in part by the Winston Chung Global Energy Center at UCR and the U.S. Department of Energy (DE-FG02-09ER16096). Yin also thanks the Research Corporation for Science Advancement for the Cottrell Scholar Award and DuPont for the Young Professor Grant. A portion of this research was conducted at the Center for Nanophase Materials Sciences, which is sponsored at Oak Ridge National Laboratory by the Division of Scientific User Facilities, Office of Basic Energy Sciences, U.S. Department of Energy.

REFERENCES

- (1) Chen, Z.; Belharouak, I.; Sun, Y. K.; Amine, K. *Adv. Funct. Mater.* 2012, 23, 959.

- (2) Deng, D.; Kim, M. G.; Lee, J. Y.; Cho, J. *Energy Environ. Sci.* **2009**, *2*, 818.
- (3) Zhu, G. N.; Wang, Y. G.; Xia, Y. Y. *Energy Environ. Sci.* **2012**, *5*, 6652.
- (4) Chen, J. S.; Tan, Y. L.; Li, C. M.; Cheah, Y. L.; Luan, D. Y.; Madhavi, S.; Boey, F. Y. C.; Archer, L. A.; Lou, X. W. *J. Am. Chem. Soc.* **2010**, *132*, 6124.
- (5) Liu, H.; Bi, Z.; Sun, X.-G.; Unocic, R. R.; Paranthaman, M. P.; Dai, S.; Brown, G. M. *Adv. Mater.* **2011**, *23*, 3450.
- (6) Wang, Y.; Su, X. W.; Lu, S. J. *Mater. Chem.* **2012**, *22*, 1969.
- (7) Lou, X. W.; Archer, L. A. *Adv. Mater.* **2008**, *20*, 1853.
- (8) Ming, J.; Wu, Y. Q.; Nagarajan, S.; Lee, D. J.; Sun, Y. K.; Zhao, F. *Y. J. Mater. Chem.* **2012**, *22*, 22135.
- (9) Park, K. S.; Min, K. M.; Jin, Y. H.; Seo, S. D.; Lee, G. H.; Shim, H. W.; Kim, D. W. *J. Mater. Chem.* **2012**, *22*, 15981.
- (10) Park, S.-J.; Kim, H.; Kim, Y.-J.; Lee, H. *Electrochim. Acta* **2011**, *56*, 5355.
- (11) Chen, J. S.; Wang, Z.; Dong, X. C.; Chen, P.; Lou, X. W. *Nanoscale* **2011**, *3*, 2158.
- (12) Liu, L.; Fan, Q.; Sun, C.; Gu, X.; Li, H.; Gao, F.; Chen, Y.; Dong, L. *J. Power Sources* **2013**, *221*, 141.
- (13) Lou, X. W.; Li, C. M.; Archer, L. A. *Adv. Mater.* **2009**, *21*, 2536.
- (14) Joo, J. B.; Zhang, Q.; Lee, I.; Dahl, M.; Zaera, F.; Yin, Y. *Adv. Funct. Mater.* **2011**, *22*, 166.
- (15) Li, N.; Zhang, Q.; Liu, J.; Joo, J.; Lee, A.; Gan, Y.; Yin, Y. *Chem. Commun.* **2013**, *49*, 5135.
- (16) Liu, J.; Qiao, S. Z.; Liu, H.; Chen, J.; Orpe, A.; Zhao, D. Y.; Lu, G. Q. *Angew. Chem., Int. Ed.* **2011**, *50*, 5947.
- (17) Joo, J. B.; Zhang, Q.; Dahl, M.; Lee, I.; Goebel, J.; Zaera, F.; Yin, Y. *Energy Environ. Sci.* **2012**, *5*, 6321.
- (18) Joo, J. B.; Lee, I.; Dahl, M.; Moon, G. D.; Zaera, F.; Yin, Y. *Adv. Funct. Mater.* **2013**, DOI: 10.1002/adfm.201300255.
- (19) Dambournet, D.; Belharouak, I.; Amine, K. *Chem. Mater.* **2010**, *22*, 1173.
- (20) Saravanan, K.; Ananthanarayanan, K.; Balaya, P. *Energy Environ. Sci.* **2010**, *3*, 939.
- (21) Hong, Z. S.; Wei, M. D.; Lan, T. B.; Jiang, L. L.; Cao, G. Z. *Energy Environ. Sci.* **2010**, *5*, 5408.
- (22) Wang, Z.; Lou, X. W. *Adv. Mater.* **2012**, *24*, 4124.
- (23) Ye, J. F.; Liu, W.; Cai, J. G.; Chen, S. A.; Zhao, X. W.; Zhou, H. H.; Qi, L. M. *J. Am. Chem. Soc.* **2011**, *133*, 933.